Super Storm Desmond: a process based assessment

Matthews T[1*], Murphy C[2], McCarthy G[3], Broderick C[2], Wilby RL[4]

*Corresponding author

[1]School of Natural Sciences and Psychology

Liverpool John Moores University

L3 3AF

United Kingdom

[2]Irish Climate Analysis and Research Units

Department of Geography

Maynooth University,

Kildare

Ireland

[3] National Oceanography Centre

Southampton

SO14 3ZH,

United Kingdom

[4]Department of Geography

Loughborough University

Loughborough

LE11 3TU

United Kingdom

Abstract

"Super" Storm Desmond broke meteorological and hydrological records during a record warm year in the British-Irish Isles (BI). The severity of the storm may be a harbinger of expected changes to regional hydroclimate as global temperatures continue to rise. Here, we adopt a process-based approach to investigate the potency of Desmond, and explore the extent to which climate change may have been a contributory factor. Through an Eulerian assessment of water vapour flux we determine that Desmond was accompanied by an Atmospheric River (AR) of severity unprecedented since at least 1979, on account of both high atmospheric humidity and high wind speeds. Lagrangian air-parcel tracking and moisture attribution techniques show that long-term warming of North Atlantic sea surface temperatures (SSTs) has significantly increased the chance of such high humidity in ARs in the vicinity of the BI. We conclude that, given exactly the same dynamical conditions associated with Desmond, the likelihood of such an intense AR has already increased by 25% due to long-term climate change. However, our analysis represents a first-order assessment, and further research is needed into the controls influencing AR dynamics.

1. Introduction

'Desmond' impacted the British-Irish Isles (BI) during 4th-6th December 2015. This extratropical cyclone was the fourth storm named jointly by the United Kingdom (UK) Met Office and Met Éireann during winter 2015/16. The storm brought strong winds (maximum gusts of 33 and 40 m s^{-1} in Ireland and the UK respectively), and delivered enough rainfall to break the 24- and 48-hour UK rainfall records (341 and 405 mm, respectively, recorded in Cumbria Northwest England; McCarthy et al., 2016). Its hydrological impacts were also extreme, with a number of UK and Irish rivers recording highest ever peak discharges (Fig 1A). Indeed, Desmond caused record-breaking outflow from Great Britain, surpassing the previous high by more than 30% (Barker et al., 2016). Overall UK damages from the storm were estimated to be £0.4-£0.5 billion (PWC, 2015). Severe storm impacts also occurred beyond the UK, including landslides in Norway (Dijkstra et al., 2016).

Such high winter BI precipitation totals and flood events are usually associated with enhanced horizontal water vapour transport from the Atlantic Ocean (Allan et al., 2016; Lavers et al., 2011). This advection occurs in narrow corridors termed 'Atmospheric Rivers' (hereafter 'ARs') embedded in the warm sector of extratropical cyclones. ARs source some of their moisture from tropical latitudes (Gimeno et al., 2014). Storm Desmond was no exception in this regard, with satellite-derived column-integrated water vapour estimates during the passage of the weather system revealing a plume of moist air connecting the BI to the sub-tropical western Atlantic (Fig. 1B). Extreme precipitation can result when such air streams are lifted orographically, as has been well documented in both North America (Neiman et al., 2008; Ralph et al., 2005) and Europe (Lavers and Villarini, 2013; Stohl et al., 2008). The conditions for orographic lifting of ARs are met along the mountainous western fringes of the BI (Fig. 1A), where (Lavers and Villarini, 2013) noted a strong correspondence between the occurrence of ARs and the timing of annual maximum precipitation events.

The amount of water vapour transported by ARs (i.e. their intensity) depends on wind speed and atmospheric moisture water content. Given that the saturation specific humidity increases by ~7%°C^{-1} according to the Clasius-Clapeyron relation, there are concerns that AR-related flooding could worsen in a warming climate. This view is supported by global climate model projections which suggest that AR frequency and intensity, driven by enhanced atmospheric moisture content, could increase for BI and coastal northwest Europe as the climate warms (Lavers et al., 2013; Ramos et al., 2016). How this translates to changing precipitation extremes is, however, somewhat more complex. For example, Shi and Durran (2016) highlight that reductions in vertical velocity, from increasing upper-level dry static stability, may act to reduce the sensitivity of extreme orographic rainfall to a warming climate.

Storm Desmond occurred during the warmest year globally since observations began, in a December that was the warmest on record for the UK (Kennedy et al., 2016). In light of these conditions, and physical reasoning – both from first-order physics and modelling – that higher air temperatures drive more intense ARs, it is tempting to invoke climate change as contributing to Desmond's severity (Oldenborgh et al., 2015). Although rainfall totals and river levels were extreme, less is known about the rarity of Desmond from a synoptic perspective. Exploring this dimension requires a process-based assessment, which has some considerable benefits. First, enhanced process understanding of the conditions driving Desmond's severity may ultimately lead to improvements in forecasting extreme hydroclimatic events. For example, Lavers et al. (2016) demonstrated the potential for information about such large-scale circulation for enhancing medium range prediction of precipitation extremes. Second, it can yield insight into the possible contribution from climate change to the exceptional hydroclimatic conditions (Trenberth et al., 2015), which in turn can enable more effective public communication of climate change impacts, and contribute to disaster risk reduction efforts (Shepherd, 2016).

Accordingly, the aim of our study is to investigate the AR associated with Storm Desmond, and to explore the role played by climate change in contributing to its severity. In what follows, the Data and Methods are provided in Section 2, results are in Section 3 and the Discussion and Conclusions are presented in Section 4.

2. Data and Methods

2.1 Data

In the subsequent sections, while all notation is introduced within the text, we include Table 2 in Supplementary Information (hereafter SI) for convenience when referring to terms featuring within equations.

We used winter half-year (October-March, 1979-2016) six-hourly data at 1°×1° spatial resolution from the ERA-Interim (ERA-I) reanalysis dataset (Dee et al., 2011) to contextualise the atmospheric circulation during Storm Desmond. ERA-I data have been used previously to identify and characterise ARs (Ramos et al., 2016), and found to agree well with other reanalysis products when used for this purpose (Lavers et al., 2012). To diagnose moisture transport, specific humidity (q), zonal (u), and meridional (v) wind components were extracted for the domain 100°W–30°E, 20°N-80°N at pressure levels 1000 to 300 hPa. Data from higher than 300 hPa in the atmosphere are neglected because little moisture is transported above this level (Ramos et al., 2016).

We also obtained six-hourly q, u, v, air temperature (T) and vertical velocity on all model levels for a global domain for winter half year, 1979-2016. These data were extracted to trace the history of air masses arriving in the BI during AR events (see Section 2.3). To this end, we additionally employed global boundary-layer height (blh) from the ERA-I surface fields, and surface pressure (ps) from the ERA-I model levels' archive. Sea-surface temperatures (SSTs) were similarly extracted for a global domain (at 1°×1° spatial resolution) from the HadISST dataset (Rayner et al., 2003) for the longer period 1870-2016. These data were used to interpret the role of SSTs in modulating the humidity of traced air parcels (Sections 2.3 and 4).

2.2 Detection and characterisation of Atmospheric Rivers

To characterise and contextualise the AR associated with Desmond, all ARs affecting the BI during the winter half year were identified using the vertically-integrated vapour transport (IVT):

$$IVT = \frac{1}{g} \int_{1000}^{300} q(u^2 + v^2)^{1/2} \, dp \qquad \text{Eq. 1}$$

where g is the acceleration due to the Earth's gravity, p denotes air pressure, and the remaining terms retain their meaning from Section 2.1.

Equation 1 was applied six-hourly to the ERA-I data. The criteria used to classify ARs were adapted from Lavers et al. (2012), who similarly classified ARs in the vicinity of the British-Irish Isles; the specifics are briefly recounted here. First, grid cells with IVT greater than the 528.2 kg m^{-1} s^{-1} threshold employed by Lavers et al. (2012) were identified as possible components of ARs. If this condition was satisfied along 10.5°W between 50 and 60°N (the approximate western fringe of the BI; Fig. 1A), a connected-neighbours algorithm was implemented to join all adjacent cells exceeding the IVT threshold (evaluated using 8-cell connectedness). If these touching cells

extended to at least 30.5°W, then the BI was defined as experiencing an AR during the respective time step. However, we only retained persistent ARs with the highest potential impact. These were defined as events lasting at least 24 hours, and whose latitude of maximum *IVT* along 10.5°W remained within 4.5° of the initial *IVT* maximum at this line of longitude. The 4.5°latitude tolerance means that the mid-point of ARs can deviate at most ~500 km from their starting position, implying sustained influence over a given region, which likely translates to greater hydrological impact. The minimum duration extent applied here is 6-hours, which is greater than employed by (Lavers et al., 2012), but was preferred for identifying ARs that were potentially most hydrologically severe. Moreover, preliminary screening of winter 2015/2016 ERA-I data indicated that Desmond's AR satisfied this time criteria.

AR intensity for each event was defined via two metrics: i) the sum of the maximum IVT along 10.5°W (50-60°N) (hereafter 'TOTAL"); and ii) the peak rolling 24-hour mean of the maximum *IVT* along the same line of longitude (hereafter "MAX24"). The former metric places weight on the total amount of moisture delivered over the lifetime of an AR, whereas the latter focuses on intensity over a 24-hour window. We also estimated the rarity of MAX24 for Desmond by calculating its return period using a Gumbel distribution, whose parameters were determined from our sample using maximum likelihood estimation. We selected the Gumbel distribution because initial screening indicated it had the minimum Akaike Information Criterion amongst a pool of candidate right-skewed distributions (see SI - for details of this provisional screening). The suitability of the fitted Gumbel distribution was evaluated using a Kolmogorov-Smirnov (KS) test, with *p*-values estimated using a Monte Carlo simulation (see Clauset et al., 2009) for a description of this procedure). It is necessary to determine *p*-values via simulation because we estimate the Gumbel distribution's parameters using sample data, which has the effect of increasing the probability of a type II error, as critical values of the KS test statistic are biased high (Steinskog et al., 2007).

The return period (R_p) for Desmond's *IVT* was estimated by evaluating:

$$R_p = \frac{1}{\zeta\,[1-CDF(IVT)]} \qquad \text{Eq. 2}$$

In which ζ is the mean number of ARs per year, and *CDF* is the Gumbel cumulative distribution function, given by:

$$CDF(IVT) = e^{-e^{-\left(\frac{IVT-\mu}{\sigma}\right)}} \qquad \text{Eq. 3}$$

where the location and scale are denoted by μ and σ, respectively. Physically, the mean of the Gumbel distribution is a linearly increasing function of both μ and σ, whereas the variance is proportional to the square of σ. We fitted the Gumbel distribution over the 1981-2010 climate period, and calculated the uncertainty on R_p using the profile likelihood method to estimate the 95% confidence interval (Coles, 2001).

To provide process insight into Desmond's AR, we separately computed the column-mean wind speed (*WS*), evaluated at the latitude of the maximum *IVT*, for the four time steps constituting MAX24:

$$WS = \frac{g}{1000-300} \int_{1000}^{300} (u^2 + v^2)^{1/2} \, dp \qquad \text{Eq. 4}$$

We also computed the total column water (*TCW*) for the same period and latitude:

$$TCW = \frac{1}{g} \int_{1000}^{300} q \, dp \qquad \text{Eq. 5}$$

which yields kg of water vapour per square meter and is equivalent to mm. The average of the four *WS* and *TCW* values were then used to characterise each AR.

2.3 Lagrangian air mass tracking

Backwards air mass tracking enables identification of sources and sinks of moisture that influence atmospheric humidity and hence the intensity of ARs (Gimeno et al., 2012; Nieto et al., 2007; Ramos et al., 2016; Winschall et al., 2014). To this end, we used the Lagrangian analysis tool 'LAGRANTO' (Sprenger and Wernli, 2015) to calculate 10-day back trajectories of air in BI ARs. We then applied the moisture accounting routine of (Sodemann et al., 2008) to identify source locations of moisture entrained in the traced air parcels. Finally, the role of SST variability in modulating AR's *TCW* was explored by calculating uptake-weighted SSTs from the HadISST dataset at sites of moisture uptake. Further details of how these analyses were implemented, including the calculation of weighted SSTs, are provided in SI.

Note that wherever we report the significance of temporal trends, their magnitudes were computed using the Seil-Then slope estimation method (which is robust to outliers; Sen, 1960; Theil, 1950), and *p*-values were evaluated using a 1,000-trial block bootstrap simulation to account for possible autocorrelation. For each trial, the Seil-Then slope was calculated for the series of randomly reordered blocks and *p* was defined as the fraction of times the absolute magnitude of these slopes exceeded the magnitude of the trend in the original series. Block lengths were determined for this procedure using the implicit equation given in (Wilks, 2011)

3. Results

3.1 Characterisation of Desmond AR

We detected 81 ARs during the 37 winter half years (Fig. 2). Desmond's AR is shown in Fig. 3 for each 6-hourly slice of passage (04/12/2015 12:00 to 06/12/2015 00:00). Maximum IVT along 10.5°W was attained on December 5th at 12:00, and the 24-hour period of peak *IVT* intensity (corresponding to MAX24) occurred from midnight on 04/12/2015 to midnight on 05/06/2015.

The other 80 ARs provide context to Desmond. According to TOTAL, Desmond's AR was ranked third since 1979, surpassed only by events in 2011 and 1991. However, by MAX24, Desmond's AR was the most severe on record (Table1). The 1991 event is the only AR other than Desmond to feature in the top three of both metrics. This AR caused heavy orographic rainfall in the Southern Pennines (Northern England), leading to river discharges with return periods estimated in excess of 100 years (Institute of Hydrology, British Geological Survey, 1992). The algorithm also detected the well-known AR in November 2009 (ranked 9th according to both metrics), an event that was also associated with flooding in both Ireland and the UK (Adger et al., 2013; Lavers et al., 2011).

The unusualness of the 24-hour *IVT* associated with Desmond was explored further by estimating the return period of MAX24 according to a Gumbel distribution. Fig (4) demonstrates the appropriateness of the Gumbel distribution, with points clustered around the 1:1 line. Confidence in the appropriateness of this distribution is increased by the KS test results, which gave little support (p=0.67) for rejecting the Gumbel as our sample's parent population. Application of Equation 2 suggested a return period of 12-66 years (95% confidence interval), with a most likely estimate of 26 years.

The representativeness of this return period rests on the MAX24 random variables being independent and identically distributed (iid). Independence seems likely, given that the minimum separation between ARs was 78 hours. It is more challenging to verify the identically distributed assumption. Global mean air temperatures have risen over the period of our AR sample

(Hartmann et al., 2013), and models indicate increasing AR intensity with climate warming (Lavers et al., 2013; Ramos et al., 2016), implying that the iid assumption may be inappropriate. However, we found no significant temporal trends in means (p=0.36) or standard deviations (p=0.13) computed on five-year running samples of MAX24 (1979-2016). Thus, the iid assumption seems to be a reasonable approximation, and we interpret the return period as representative for the climate of the recent past.

Further insight into the unusualness of Desmond's MAX24 relative to the rest of the ARs was explored by assessing *WS* and *TCW* separately over the 24 hours of maximum intensity (Table 2). Neither of these quantities was unprecedented, but both approached the upper end of their distributions, with empirical non-exceedance probabilities of 88.9 and 92.6% for *TCW* and *WS* respectively (Fig. 5). *TCW* for Desmond is perhaps more unusual when the timing is considered, as only two of the top 10 events by *TCW* occur outside of October and November, which is physically consistent with the higher SSTs that prevail during these autumn months. By contrast, Desmond was less seasonally unusual in terms of *WS*, as all but one of the top 10 events by this metric occurred in the core winter months (December to February), with six falling in December. The result of concurrent extremes in these quantities means that Desmond's AR is ranked top if the products of the 24-hour average *WS* and *TCW* are assessed (not shown). Whilst this result is consistent with the analysis of MAX24, it should not be regarded self-evident, as the latter depends on covariations between q and u/v (Equation 1), which are not captured by equations 4 and 5.

3.1 Lagrangian air mass tracking and moisture attribution

Back trajectories from the region of maximum *IVT* are shown in Fig. 6. Across all ARs, incident air parcels evidently spend much of their time to the west of the BI. The majority of the air parcels' time is, however, spent over the North Atlantic and Desmond was no exception in this regard (Fig. 6b). For all tracks, we could attribute an average of 50% of moisture to source regions (see SI for context regarding 'unattributed' moisture), somewhat lower than that reported by (Sodemann et al., 2008). We explore reasons for this in Section 4. Most moisture uptake occurs over the North Atlantic (Fig. 6c), with the location of the maxima following the path of the Gulf Stream extension near 40°N.

To explore SST influence on *TCW* we computed the mean SST at uptake locations for each AR during the period of MAX24. Fig. 7 indicates a highly significant correlation (r=0.62; p<0.001) between mean SST and corresponding mean *TCW*, with a sensitivity (β) of 1.16 ± 0.17 mm °C^{-1}. We calculate the lowest mean SST experienced by air entrained in all ARs to be 13.1°C, and the highest to be 22.6°C, translating to a difference in *TCW* of around 11 mm (43% of the mean *TCW* across all ARs) using this regression equation. Air parcels entrained in Desmond's AR encountered a mean SST of 19.7°C, higher than 75% of all other ARs assessed. Evaluating the regression function at this x-coordinate (assuming normally distributed residuals whose standard deviation is 3.15 mm; see Fig. 7 annotation), yields a conditional exceedance probability of *TCW* as high as experienced during Desmond (30 mm; hereafter *DTCW*) of 18%, which is 55% greater than the marginal probability (of 11.1%; given by 100-88.9%; see Fig. 5).

We have, therefore, demonstrated empirically that SSTs experienced by incident air parcels exert control on the *TCW*. This raises an interesting question about the possible role of climate change in increasing the likelihood of attaining *DTCW*. Variability in SSTs experienced by air entrained in ARs may result from (1) the positions of the boundary-layer tracks themselves (for example, tracks spending more time over the lower latitude North Atlantic are more likely to experience warmer SSTs); and (2) temporal variability in SSTs, resulting from internal variability at a range

of time scales, and also from externally-forced climate warming. Under constant (1), long-term increases in SSTs would be expected to increase the likelihood of *DTCW* (cf. Fig. 7).

To explore the role of climate warming in contributing to Desmond's high *TCW*, we implemented an experiment that isolated (2). We took the observed air parcel trajectories (and uptake locations/amounts) from Storm Desmond and iteratively replaced the observed 2015 SST field with SSTs from all years in the HadISST dataset (1870-2015). The mean SST experienced by the air parcels for each of these alternative scenarios was then calculated from SI Equation 3, with the resulting SSTs used to compute conditional exceedance probabilities (pr_2) for *DTCW,* using the regression equation (Fig. 7). These probabilities were compared to the reference value (pr_1) obtained for the 2015 SST field (18% - see above). An upward trend in the ratio pr_2/pr_1 (hereafter 'PR' – the Probability Ratio; Fischer and Knutti, 2015) would result from increasing SSTs along Desmond's boundary layer air parcel trajectories. This experiment is warranted because the result is far from a forgone conclusion: global mean December SSTs have risen by almost 0.4°C/Century, increasing to more than 0.5°C/Century if the trend is computed from the early 20th Century (Fig. 8A). However, warming has been much suppressed over a large area of the North Atlantic, with cooling even apparent in the region of the sub-polar gyre (Fig. 8 A and B). Accordingly, around 32% of Desmond's moisture uptake occurred from regions with SSTs below their 1951-1980 mean during December 2015 (Fig. 8 C and D). Our experiment therefore permits insight into how much warmer the track-averaged SSTs could have been in other years with less pronounced cool SST anomalies. We adopt the 1951-1980 climate normal period because it has been used widely as a reference, and the Atlantic Multidecadal Oscillation (Kushnir, 1994) was approximately neutral during this time.

This experiment indicates that uptake-weighted mean SSTs along Desmond's track have risen since 1870, with a significant upward trend of 0.37±0.12°C Century^{-1} (Fig. 9). This rate is approximately equal to the global mean (Fig. 8 A) and slightly less than the trend in mean North Atlantic SSTs (0.40±0.04°C Century^{-1}: calculated over the region -80-5°E, 0-70°N using weights based on grid cell surface area, accounting for unequal cell sizes). The increasing SSTs along Desmond's track translate into a significant rise of 17% Century^{-1} in PR (~25% since 1870)*.* However, despite the increasing trend, pronounced high- and low-frequency variability in along-track SSTs means that, for identical air parcel trajectories, higher SSTs (and inferred *TCW*) should have been expected for Desmond's AR in 15 other years since 1870, and the rolling 30-year mean SST was actually at a peak during the middle of the 20th Century (centred on 1947).

4. Discussion and Conclusions

Our results suggest that the record precipitation and river discharge observed during the passage of Storm Desmond was associated with an AR of unprecedented intensity since at least 1979. This finding is consistent with previous work that has highlighted the importance of ARs in driving hydrological extremes along the western margins of the North Atlantic (Allan et al., 2016; Lavers et al., 2011; Liberato et al., 2012; Stohl et al., 2008; Trigo et al., 2014). To date, the extreme rainfall associated with Storm Desmond's passage has been attributed to a slow-moving trailing front and the advection of a very mild and moist air mass (McCarthy et al., 2016). Our results highlight the latter as being particularly important; Desmond's AR was most remarkable for its 24-hour intensity (MAX24), rather than the total moisture flux over its lifetime (TOTAL). We have deepened process understanding of the extraordinary nature of this intense episode of vapour transport by indicating that it was due to a combination of both a humid air mass, *and* its rapid advection. The former was particularly marked for an AR making BI landfall during December.

The unusually high *TCW* during Desmond's AR is particularly interesting given that it is the long-term increase in atmospheric humidity, driven by rising SSTs, that is credited with increasing the AR hazard as the climate warms (Lavers et al., 2013). In this context, the severity of Desmond's AR could be interpreted as consistent with the observed long-term warming. However, such a simple interpretation is confounded by the fact that air entrained in ARs can encounter very different trajectories and SSTs at moisture uptake locations whilst on-route to the BI. Moreover, whilst global SSTs have increased, the North Atlantic region has exhibited more complex evolution of the SST field.

To isolate the possible role that climate warming may have played in raising the probability of such an intense AR, we removed dynamical variability by fixing air parcel trajectories and uptake locations to those observed during Desmond. This provided an assessment of how the SSTs along Desmond's unique track have evolved, and thus how, given exactly the same dynamical setup, the probability of such an intense AR may have changed over time. We find that SSTs within the region of the NA sampled by air parcels entrained within Desmond *have* experienced significant warming since 1870. Accordingly, we infer that the probability of *DTCW* (conditional on the dynamical setup) has increased significantly over the observational period. Note that we cannot strictly attribute this rising probability to anthropogenic forcing because our observational methodology does not distinguish amongst candidate *drivers* of long-term SST increase. However, research to date has found that, across the North Atlantic, only climate models (in the Coupled Model Inter-comparison Project Stage 5) which include all anthropogenic forcing mechanisms can reproduce the observed basin-wide positive trend in ocean heat content (Bindoff et al., 2013). This lends support to the prospect that the rising SSTs and probability of *DTCW* are indeed anthropogenically forced. Future research repeating our Lagrangian moisture attribution analysis using *factual* vs. *counterfactual* modelled SSTs could add greater confidence to this conclusion (Shepherd, 2016).

We acknowledge, however, that our finding of increasing *DTCW* probability rests on some caveats. First, the Lagrangian attribution technique identified only around 50% of moisture sources. This is less than the 66% attained by Sodemann et al. (2008), but is consistent with the more restrictive conditions under which we have applied their algorithm. The authors of this moisture-tracking routine cite neglect of turbulence, convection, and evaporation from precipitating hydrometeors among its limitations. Within ARs these conditions are likely to be encountered more frequently, as entrained air travels in close proximity to atmospheric fronts characterised by static instability and precipitation.

A second caveat is that our treatment to control for dynamical variability is simplistic. In applying the regression function (Fig. 7) to infer the impact of changing SSTs on *DTCW,* we imply that SST variability has no impact on the atmospheric circulation of Storm Desmond. That is, the locations and amount of moisture uptake (evaporation) and loss (precipitation) are assumed to remain constant. In reality, changing SSTs could also be expected to influence these aspects of Storm Desmond. More complete insight into the influence of SST warming on Desmond's AR in this regard could be gained through appropriately-designed experiments within numerical weather models, which account for the complex interaction between atmospheric circulation and SSTs (Lackmann, 2014; Meredith et al., 2015). We emphasise that out analysis simply confirms that uptake-weighted mean SST experienced by air entrained in ARs does indeed correlate with *TCW* at landfall, and we observed that despite the complex SST evolution over the North Atlantic, SSTs have risen significantly at the uptake locations associated with Desmond's AR.

In addition to the long-term upward trend in SSTs at Desmond's moisture uptake locations, our analysis also highlighted pronounced SST variability, with 15 other years yielding increased

probability of *DTCW,* and the rolling 30-year maximum occurring in the middle of the 20th Century. The latter mainly reflects the basin-wide, low-frequency variability in SSTs described by the AMO, which was in a positive (warm) phase during the period 1930-1960 before turning negative until around 2000 (Trenary and DelSole, 2016). Our most recent 30-year running-mean SSTs were, therefore, calculated for a period encompassing both negative and positive AMO states.

We further note that, whilst SSTs along Desmond's track have increased significantly, (translating to a rise in PR), the magnitude of this change is modest compared to variability in SSTs observed *between* ARs (~10°C SST difference between ARs, *versus* ~0.5°C SST warming along Desmond's AR track 1870-2015; figs 7 and 9). This highlights the importance of dynamical variability in explaining AR intensity, and is therefore consistent with the earlier observation (when examining the iid assumption) of no recent trend in MAX24 despite global warming. The evolving severity of ARs over the observational period – particularly in terms of *TCW* – is best understood in terms of the prevailing atmospheric circulation, rather than concurrent long-term thermodynamic changes in the climate system.

In this context, we suggest that future studies should explore controls on these dynamics in more detail. Although research has established a connection between the phase of the North Atlantic Oscillation and the number of BI ARs (Brands et al., 2017; Lavers and Villarini, 2013), less is known about how such modes of variability may influence the intensity of ARs through modifying air parcel trajectories and moisture uptake locations. The AMO may also play an important role in this respect. Not only does it directly affect moisture uptake (through elevated SSTs), it also modulates North Atlantic atmospheric circulation (McCarthy et al., 2015; Peings and Magnusdottir, 2014). The AMO's predictability at lead times of up to a decade (Mochizuki et al., 2012), raises the prospect of forecasting periods of enhanced AR hazard with considerable lead time. The recent release of centennial records of North Atlantic ARs (Brands et al., 2017) opens a way to examine these possible controls in the near future.

In closing, we summarise that our research has explained the severity of Storm Desmond from a process-based perspective, highlighting empirically the role of SSTs in modulating AR moisture. Accordingly, we interpret that long-term North Atlantic warming may have increased the chance of an AR as severe as in Storm Desmond. This conclusion may help provide a tangible, easily communicated example for wider dissemination, of the impacts from climate change on North Atlantic hydroclimatic extremes. Further, we are hopeful that, in addressing the influence of SSTs on AR moisture content, our results may encourage exploring SST forcing of AR severity in more detail, including any influence on dynamics. We are hopeful that such understanding may eventually improve prediction of extreme events and ultimately contribute to risk reduction efforts.

Acknowledgements

References

Adger, W.N., Quinn, T., Lorenzoni, I., Murphy, C., Sweeney, J., 2013. Changing social contracts in climate-change adaptation. Nat. Clim. Change 3, 330–333. doi:10.1038/nclimate1751

Allan, R.P., Lavers, D.A., Champion, A.J., 2016. Diagnosing links between atmospheric moisture and extreme daily precipitation over the UK. Int. J. Climatol. 36, 3191–3206. doi:10.1002/joc.4547

Barker, L., Hannaford, J., Muchan, K., Turner, S., Parry, S., 2016. The winter 2015/2016 floods in the UK: a hydrological appraisal. Weather 71, 324–333. doi:10.1002/wea.2822

Bindoff, N.L., Stott, P.A., AchutaRao, M.R., Allen, M.R., Gillett, N., Gutzler, D., Hansingo, K., Hegerl, G., Hu, Y., Jain, S., Mokhov, I.I., Overland, J., Perlwitz, J., Sebbari, R., Zhang, X., 2013. Detection and Attribution of Climate Change: from Global to Regional, in: Climate Change 2013: The Physical Science Basis. Contribution of Working Group I to the Fifth Assessment Report of the Intergove Rnmental Panel on Climate Change. Cambridge University Press, Cambridge, United Kingdom and New York, NY, USA, pp. 867–952.

Brands, S., Gutiérrez, J.M., San-Martín, D., 2017. Twentieth-century atmospheric river activity along the west coasts of Europe and North America: algorithm formulation, reanalysis uncertainty and links to atmospheric circulation patterns. Clim. Dyn. 48, 2771–2795. doi:10.1007/s00382-016-3095-6

Clauset, A., Shalizi, C.R., Newman, M.E.J., 2009. Power-Law Distributions in Empirical Data. SIAM Rev. 51, 661–703. doi:10.2307/25662336

Coles, S., 2001. An introduction to statistical modeling of extreme values. Springer, London.

Danielson, J., Gesch, D., 2011. Global Multi-resolution Terrain Elevation Data 2010 (GMTED2010) - of2011-1073.pdf (No. 2011–1073), US Geological Survey Open File Report.

Dee, D.P., Uppala, S.M., Simmons, A.J., Berrisford, P., Poli, P., Kobayashi, S., Andrae, U., Balmaseda, M.A., Balsamo, G., Bauer, P., Bechtold, P., Beljaars, A.C.M., van de Berg, L., Bidlot, J., Bormann, N., Delsol, C., Dragani, R., Fuentes, M., Geer, A.J., Haimberger, L., Healy, S.B., Hersbach, H., Hólm, E.V., Isaksen, L., Kållberg, P., Köhler, M., Matricardi, M., McNally, A.P., Monge-Sanz, B.M., Morcrette, J.-J., Park, B.-K., Peubey, C., de Rosnay, P., Tavolato, C., Thépaut, J.-N., Vitart, F., 2011. The ERA-Interim reanalysis: configuration and performance of the data assimilation system. Q. J. R. Meteorol. Soc. 137, 553–597. doi:10.1002/qj.828

Dijkstra, T., Freeborough, K., Reeves, H., Nykjaer, B.S., Sund, M., Devoli, G., Banks, V., 2016. Landslide response signatures from storm Desmond (UK)/Synne (Norway), December 2015. Presented at the EGU General Assembly Conference Abstracts, p. 16411.

Fischer, E.M., Knutti, R., 2015. Anthropogenic contribution to global occurrence of heavy-precipitation and high-temperature extremes. Nat. Clim. Change 5, 560–564. doi:10.1038/nclimate2617

Gimeno, L., Nieto, R., Vázquez, M., Lavers, D.A., 2014. Atmospheric rivers: a mini-review. Front. Earth Sci. 2. doi:10.3389/feart.2014.00002

Gimeno, L., Stohl, A., Trigo, R.M., Dominguez, F., Yoshimura, K., Yu, L., Drumond, A., Durn-Quesada, A.M., Nieto, R., 2012. Oceanic and terrestrial sources of continental precipitation. Rev. Geophys. 50, 1–41. doi:10.1029/2012RG000389

Hartmann, D.L., Klein Tank, A.M.G., Rusticucci, M., Alexander, L.V., Brönnimann, S., Charabi, Y., Dentener, F.J., Dlugokencky, E.J., Easterling, D.R., Kaplan, A., Soden, B.J., Thorne, P.W., Wild, M., Zhai, P.M., 2013. Observations: Atmosphere and Surface, in: The Physical Science Basis. Contribution of Working Group I to the Fifth Assessment Report of the Intergovernmental Panel on Climate Change [Stocker, T.F., D. Qin, G.-K. Plattner, M. Tignor, S.K. Allen, J. Boschung, A. Nauels, Y. Xia, V. Bex and P.M. Midgley (Eds.). Cambridge University Press, Cambride, United Kingdom and New York, NY, USA.

Haylock, M.R., Hofstra, N., Klein Tank, A.M.G., Klok, E.J., Jones, P.D., New, M., 2008. A European daily high-resolution gridded data set of surface temperature and precipitation for 1950–2006. J. Geophys. Res. Atmospheres 113, D20119. doi:10.1029/2008JD010201

Institute of Hydrology, British Geological Survey, 1992. Hydrological data United Kingdom 1991 Yearbook: an account of rainfall, river flows, groundwater levels and river water quality January to December 1991. Wallingford, NERC Institute of Hydrology.

Kennedy, J., Morice, C., Parker, D., Kendon, M., 2016. Global and regional climate in 2015. Weather 71, 185–192. doi:10.1002/wea.2760

Kushnir, Y., 1994. Interdecadal Variations in North Atlantic Sea Surface Temperature and Associated Atmospheric Conditions. J. Clim. 7, 141–157. doi:10.1175/1520-0442(1994)007<0141:IVINAS>2.0.CO;2

Lackmann, G.M., 2014. Hurricane Sandy before 1900 and after 2100. Bull. Am. Meteorol. Soc. 96, 547–560. doi:10.1175/BAMS-D-14-00123.1

Lavers, D.A., Allan, R.P., Villarini, G., Lloyd-Hughes, B., Brayshaw, D.J., Wade, A.J., 2013. Future changes in atmospheric rivers and their implications for winter flooding in Britain. Environ. Res. Lett. 8, 034010. doi:10.1088/1748-9326/8/3/034010

Lavers, D.A., Allan, R.P., Wood, E.F., Villarini, G., Brayshaw, D.J., Wade, A.J., 2011. Winter floods in Britain are connected to atmospheric rivers. Geophys. Res. Lett. 38, L23803. doi:10.1029/2011GL049783

Lavers, D.A., Pappenberger, F., Richardson, D.S., Zsoter, E., 2016. ECMWF Extreme Forecast Index for water vapor transport: A forecast tool for atmospheric rivers and extreme precipitation. Geophys. Res. Lett. 43, 2016GL071320. doi:10.1002/2016GL071320

Lavers, D.A., Villarini, G., 2013. The nexus between atmospheric rivers and extreme precipitation across Europe. Geophys. Res. Lett. 40, 3259–3264. doi:10.1002/grl.50636

Lavers, D.A., Villarini, G., Allan, R.P., Wood, E.F., Wade, A.J., 2012. The detection of atmospheric rivers in atmospheric reanalyses and their links to British winter floods and the large-scale climatic circulation. J. Geophys. Res. Atmospheres 117, 1–13. doi:10.1029/2012JD018027

Liberato, M.L.R., Ramos, A.M., Trigo, R.M., Trigo, I.F., Durán-Quesada, A.M., Nieto, R., Gimeno, L., 2012. Moisture Sources and Large-Scale Dynamics Associated With a Flash Flood Event, in: Lin, J., Brunner, D., Gerbig, C., Stohl, A., Luhar, A., Webley, P. (Eds.), Lagrangian Modeling of the Atmosphere. American Geophysical Union, pp. 111–126. doi:10.1029/2012GM001244

McCarthy, G.D., Haigh, I.D., Hirschi, J.J.-M., Grist, J.P., Smeed, D.A., 2015. Ocean impact on decadal Atlantic climate variability revealed by sea-level observations. Nature 521, 508–510. doi:10.1038/nature14491

McCarthy, M., Spillane, S., Walsh, S., Kendon, M., 2016. The meteorology of the exceptional winter of 2015/2016 across the UK and Ireland. Weather 71, 305–313. doi:10.1002/wea.2823

Meredith, E.P., Semenov, V.A., Maraun, D., Park, W., Chernokulsky, A.V., 2015. Crucial role of Black Sea warming in amplifying the 2012 Krymsk precipitation extreme. Nat. Geosci. 8, 615–619. doi:10.1038/ngeo2483

Mochizuki, T., Chikamoto, Y., Kimoto, M., Ishii, M., Tatebe, H., Komuro, Y., Sakamoto, T.T., Watanabe, M., Mori, M., 2012. Decadal Prediction Using a Recent Series of MIROC Global Climate Models. 気象集誌 第 2 輯 90A, 373–383. doi:10.2151/jmsj.2012-A22

Neiman, P.J., Ralph, F.M., Wick, G.A., Lundquist, J.D., Dettinger, M.D., 2008. Meteorological Characteristics and Overland Precipitation Impacts of Atmospheric Rivers Affecting the West Coast of North America Based on Eight Years of SSM/I Satellite Observations. J. Hydrometeorol. 9, 22–47. doi:10.1175/2007JHM855.1

Nieto, R., Gimeno, L., Gallego, D., Trigo, R., 2007. Contributions to the moisture budget of airmasses over Iceland. Meteorol. Z. 16, 37–44. doi:10.1127/0941-2948/2007/0176

Oldenborgh, G.J., Otto, F., Haustein, K., Cullen, H., 2015. Climate change increases the probability of heavy rains like those of storm Desmond in the UK - an event attribution study in near real time. Hydrol. Earth Syst. Scienes 12, 13197–13216.

Peings, Y., Magnusdottir, G., 2014. Forcing of the wintertime atmospheric circulation by the multidecadal fluctuations of the North Atlantic ocean. Environ. Res. Lett. 9, 034018. doi:10.1088/1748-9326/9/3/034018

PWC [WWW Document], 2015. . PWC. URL http://pwc.blogs.com/press_room/2015/12/updated-estimates-on-cost-of-storm-desmond-pwc.html (accessed 5.25.17).

Ralph, F.M., Neiman, P.J., Rotunno, R., 2005. Dropsonde Observations in Low-Level Jets over the Northeastern Pacific Ocean from CALJET-1998 and PACJET-2001: Mean Vertical-Profile

and Atmospheric-River Characteristics. Mon. Weather Rev. 133, 889–910. doi:10.1175/MWR2896.1

Ramos, A.M., Tomé, R., Trigo, R.M., Liberato, M.L.R., Pinto, J.G., 2016. Projected changes in atmospheric rivers affecting Europe in CMIP5 models. Geophys. Res. Lett. doi:10.1002/2016GL070634

Rayner, N.A., Parker, D.E., Horton, E.B., Folland, C.K., Alexander, L.V., Rowell, D.P., Kent, E.C., Kaplan, A., 2003. Global analyses of sea surface temperature, sea ice, and night marine air temperature since the late nineteenth century. J. Geophys. Res. 108, 4407. doi:10.1029/2002JD002670

Sen, P.K., 1960. On Some Convergence Properties of U-Statistics. Calcutta Stat. Assoc. Bull. 10, 1–18. doi:10.1177/0008068319600101

Shepherd, T.G., 2016. A Common Framework for Approaches to Extreme Event Attribution. Curr. Clim. Change Rep. 2, 28–38. doi:10.1007/s40641-016-0033-y

Shi, X., Durran, D., 2016. Sensitivities of Extreme Precipitation to Global Warming Are Lower over Mountains than over Oceans and Plains. J. Clim. 29, 4779–4791. doi:10.1175/JCLI-D-15-0576.1

Sodemann, H., Schwierz, C., Wernli, H., 2008. Interannual variability of Greenland winter precipitation sources: Lagrangian moisture diagnostic and North Atlantic Oscillation influence. J. Geophys. Res. Atmospheres 113, D03107. doi:10.1029/2007JD008503

Sprenger, M., Wernli, H., 2015. The LAGRANTO Lagrangian analysis tool – version 2.0. Geosci Model Dev 8, 2569–2586. doi:10.5194/gmd-8-2569-2015

Steinskog, D.J., Tjøstheim, D.B., Kvamstø, N.G., 2007. A Cautionary Note on the Use of the Kolmogorov–Smirnov Test for Normality. Mon. Weather Rev. 135, 1151–1157. doi:10.1175/MWR3326.1

Stohl, A., Forster, C., Sodemann, H., 2008. Remote sources of water vapor forming precipitation on the Norwegian west coast at 60°N–a tale of hurricanes and an atmospheric river. J. Geophys. Res. Atmospheres 113, D05102. doi:10.1029/2007JD009006

Theil, H., 1950. A Rank-Invariant Method of Linear and Polynomial Regression Analysis. K. Ned. Akad. Var Wet. Proc. 53, 386–392. (Part 1), 521–525 (Part 2), 1397–1412 (Part 3).

Trenary, L., DelSole, T., 2016. Does the Atlantic Multidecadal Oscillation Get Its Predictability from the Atlantic Meridional Overturning Circulation? J. Clim. 29, 5267–5280. doi:10.1175/JCLI-D-16-0030.1

Trenberth, K.E., Fasullo, J.T., Shepherd, T.G., 2015. Attribution of climate extreme events. Nat. Clim. Change 5, 725–730. doi:10.1038/nclimate2657

Trigo, R.M., Varino, F., Ramos, A.M., Valente, M.A., Zêzere, J.L., Vaquero, J.M., Gouveia, C.M., Russo, A., 2014. The record precipitation and flood event in Iberia in December 1876: description and synoptic analysis. Front. Earth Sci. 2. doi:10.3389/feart.2014.00003

Wentz, F.J., Spencer, R.W., 1998. SSM/I Rain Retrievals within a Unified All-Weather Ocean Algorithm. J. Atmospheric Sci. 55, 1613–1627. doi:10.1175/1520-0469(1998)055<1613:SIRRWA>2.0.CO;2

Wilks, D.S., 2011. Statistical Methods in the Atmospheric Sciences. Academic Press.

Winschall, A., Pfahl, S., Sodemann, H., Wernli, H., 2014. Comparison of Eulerian and Lagrangian moisture source diagnostics - The flood event in eastern Europe in May 2010. Atmospheric Chem. Phys. 14, 6605–6619. doi:10.5194/acp-14-6605-2014

Figure and Tables

Table 1. Rankings of ARs according to IVT summed over their full duration (TOTAL), and the peak 24-hour mean IVT attained during the ARs' lifetime (MAX24). Note that the date corresponds to the earliest time step of the AR.

TOTAL			MAX24		
Date	$\sum$ IVT (kg m^{-1} s^1)	Rank	Date	IVT (kg m^{-1} s^1)	Rank
08/10/2011	9942	1	**04/12/2015**	**1128**	**1**
20/12/1991	7414	2	20/12/1991	1098	2
04/12/2015	**7370**	**3**	09/11/2015	1073	3
03/02/2011	7290	4	14/12/1982	1034	4
31/12/1991	7004	5	26/12/1983	1032	5
26/12/1994	6559	6	25/10/2008	1029	6
11/02/1998	6522	7	08/10/2011	1026	7
13/02/1990	6222	8	06/03/2015	1018	8
18/11/2009	6158	9	18/11/2009	1014	9
25/12/2011	5724	10	10/12/1994	1009	10

Table 2. ARs ranked by column-mean wind speed (*WS*) and total column water (*TCW*) at the latitude of maximum integrated vapour transport (*IVT*) along 10.5°W (50-60°N) averaged over the 24-hour period corresponding to maximum *IVT* intensity.

| Rank	*WS* Date	*WS* m s^{-1}	*TCW* Date	*TCW* (mm)
1	31/12/1983	43.1	09/10/2008	36.0
2	04/02/1990	40.5	09/10/2011	34.1
3	06/02/1984	40.1	05/10/1990	33.3
4	21/12/1991	39.8	21/10/1986	32.0
5	14/12/1982	39.8	18/11/2009	31.4
6	27/10/1998	39.4	29/11/2001	31.4
7	**05/12/2015**	39.3	22/12/2012	30.4
8	01/01/1992	39.3	13/11/1994	30.4
9	29/12/2004	39	07/10/1984	30.1
10	27/12/1983	39.0	**05/12/2015**	**30.0**
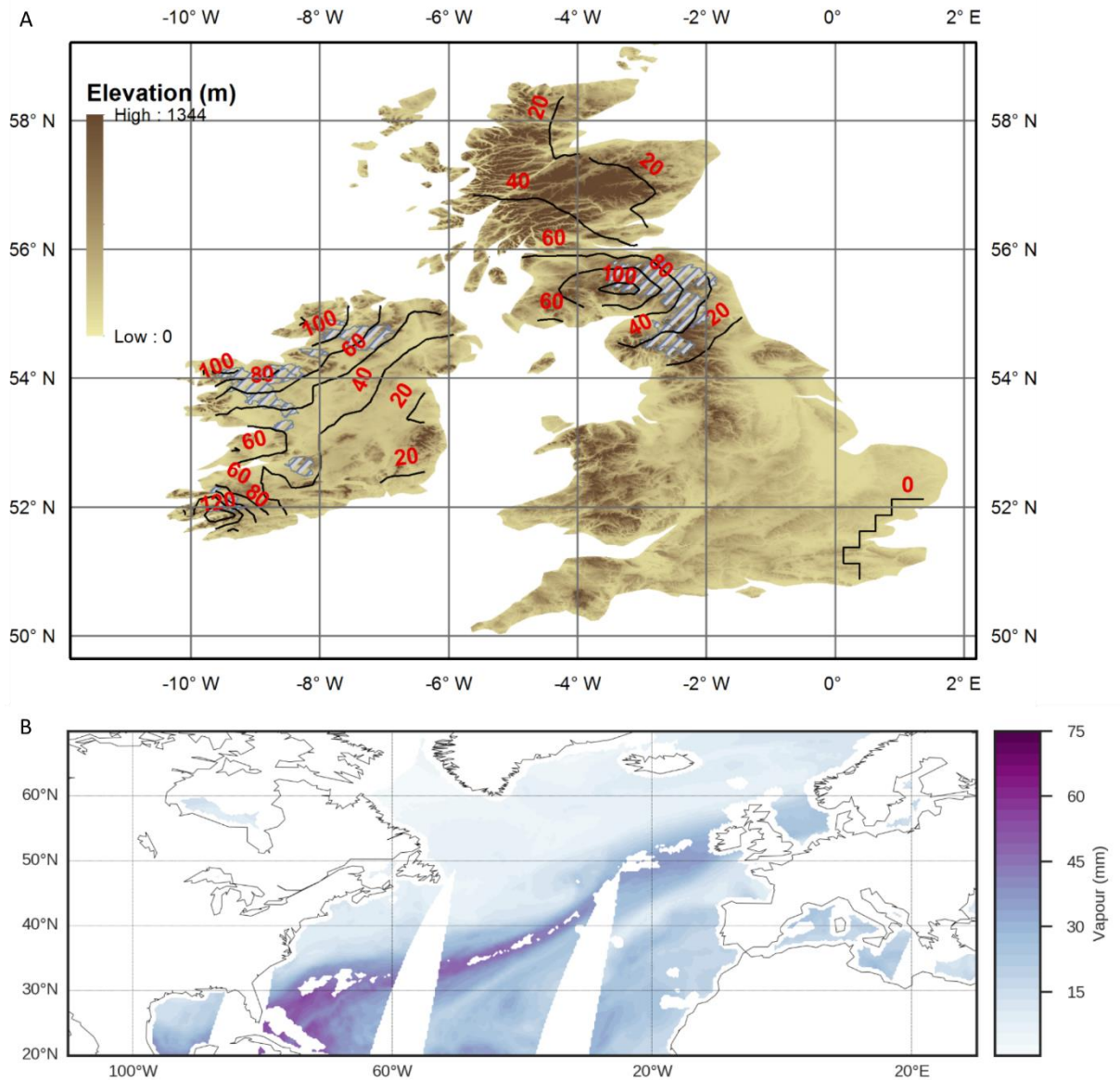
Figure 1 . BI context in relation to Storm Desmond. A: 7.5 arc-second DEM from global multi-resolution terrain elevation data (Danielson and Gesch, 2011). Polygons mark the river catchments that experienced record discharge from Storm Desmond: UK catchments are identified from Barker et al. (2016); Republic of Ireland catchments are identified using records from the Office of Public Works (see Supplementary Information). The contour field gives daily precipitation totals (mm) for December 5th, 2015, according to the E-Obs dataset (Haylock et al., 2008). B: Special Sensor Microwave Image/Sounder (SSMIS) F16 retrievals of column integrated water vapour (Wentz and Spencer, 1998) on the ascending orbit on 5th December, 2015. Note that white areas indicate no data.
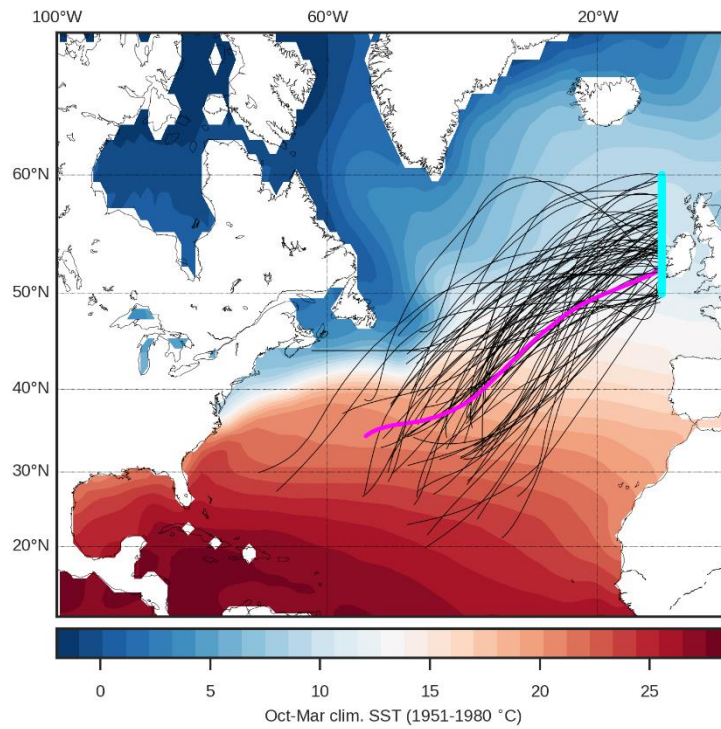
Figure 2. Axes of the 81 ARs identified by tracing local maxima of IVT northwest, west, southwest, and south from the ARs peak value along 10.5°W (50-60°N). Note that Desmond's AR is highlighted in magenta. All tracks were smoothed using a 3rd order Savitzky-Golay filter (Savitsky and Golay, 1964) for final plotting. The filter replaces each *y* quantity (AR latitude) with a value determined by a local (3rd order) polynomial fit of *y* as a function of *x* (AR longitude). In this instance, we use a 31-term window to fit the local polynomials.
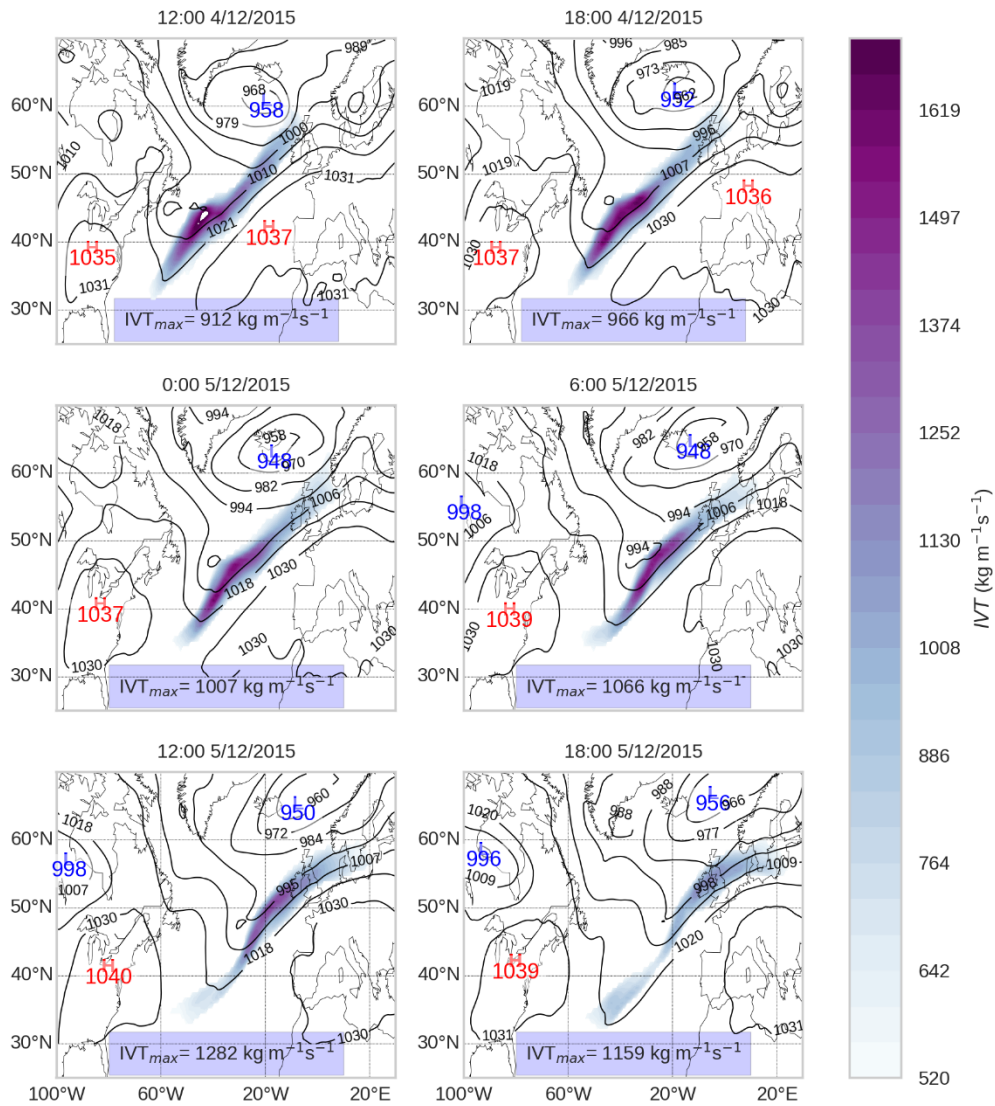
Figure 3. IVT during the lifetime of Desmond's AR. The mean sea-level pressure is also plotted (black contours) with local high- and low- centres marked along with their central pressure (hPa). Note that the low associated with storm Desmond is in the vicinity of Iceland.
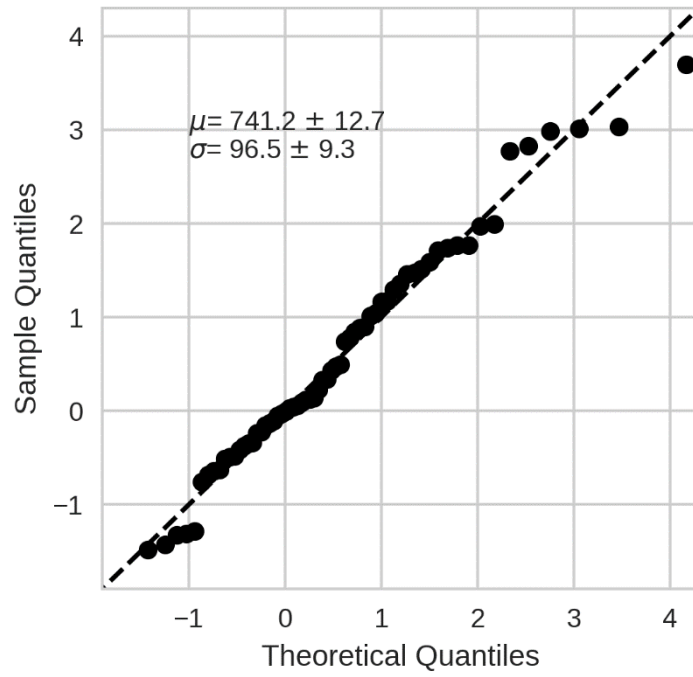
Figure 4. Quantile-Quantile (QQ) plot illustrating the goodness of fit between 1981-2010 MAX24 and the fitted Gumbel distribution, whose parameters (± standard error) are annotated on the plot.
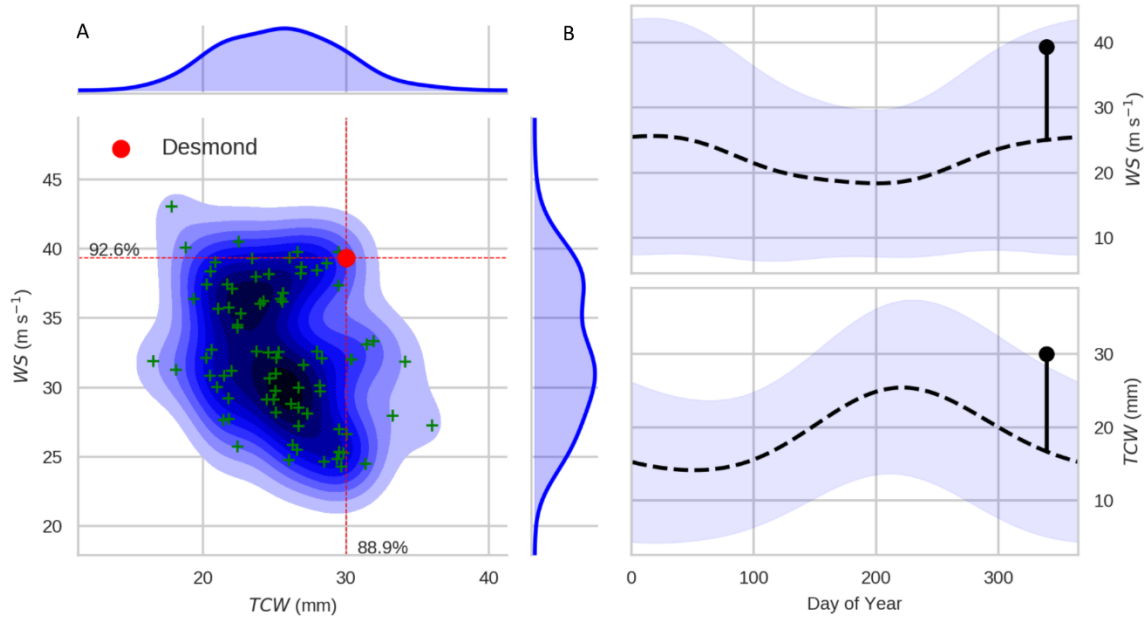
Figure 5. Column-mean wind speed (*WS;* Equation 4) and Total column water (*TCW*; Equation 5) in ARs. A: bivariate scatter of each AR's *TCW* versus its mean wind speed. The green crosses represent conditions during each AR, whilst the blue shading summarises the two-dimensional density. Note that the red, dotted lines highlight the empirical non-exceedance probabilities for Desmond. The blue curves (top and centre) show the kernel-density estimates of the marginal distributions of *TCW* and *WS*, respectively. B: seasonal mean profile of *WS* and *TCW* along 10.5°W (50-60°N) over the period 1981-2010 (dotted line), with Desmond's *TCW* and *WS* (averaged over the period of MAX24) marked with vertical bar. Note that the shaded region spans ± one standard deviation of the seasonal mean profile.
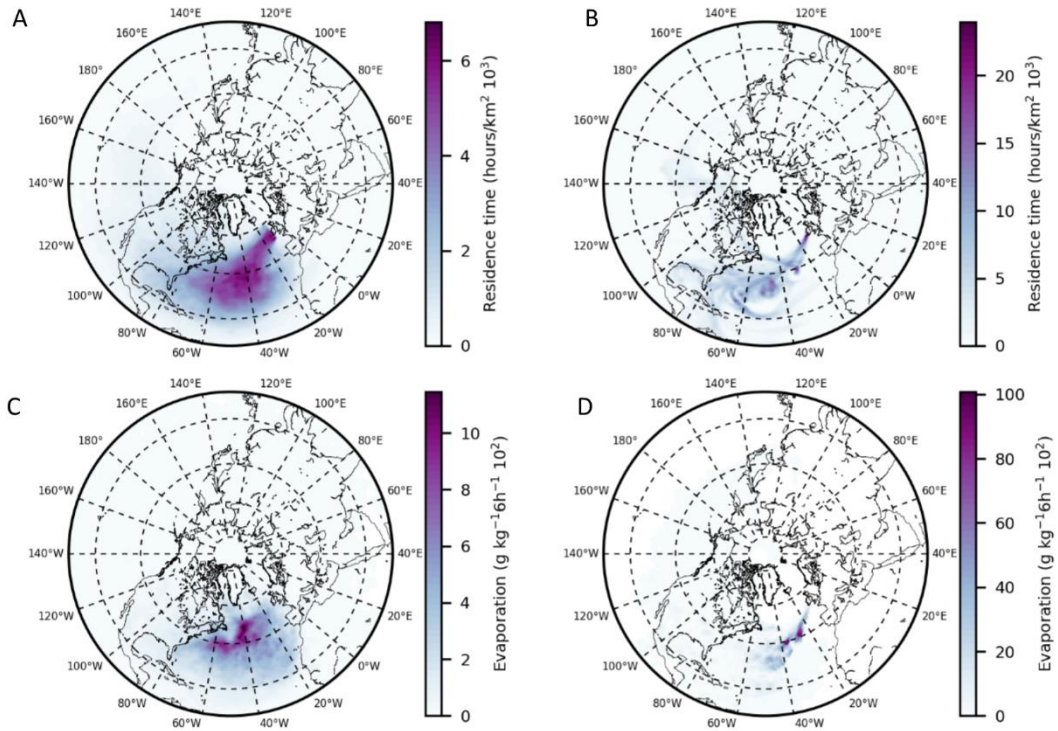
Figure 6. A: residence time of air parcels traced backwards (over a ten-day period) for all ARs. Residence time is a function of the number of air parcels passing over a point, and how long they are located over this region. B: same as A but only for air parcels traced backwards during the 24-hour period of max *IVT* for Desmond. C: attributed moisture amounts evaporated into back-traced air parcels. D: same as A but only for air parcels traced backwards during the 24-hour period of max *IVT* for Desmond. Note that the stereographic projections are bounded at 10°N, with dashed lines marking 20° increments from 20-80°N.
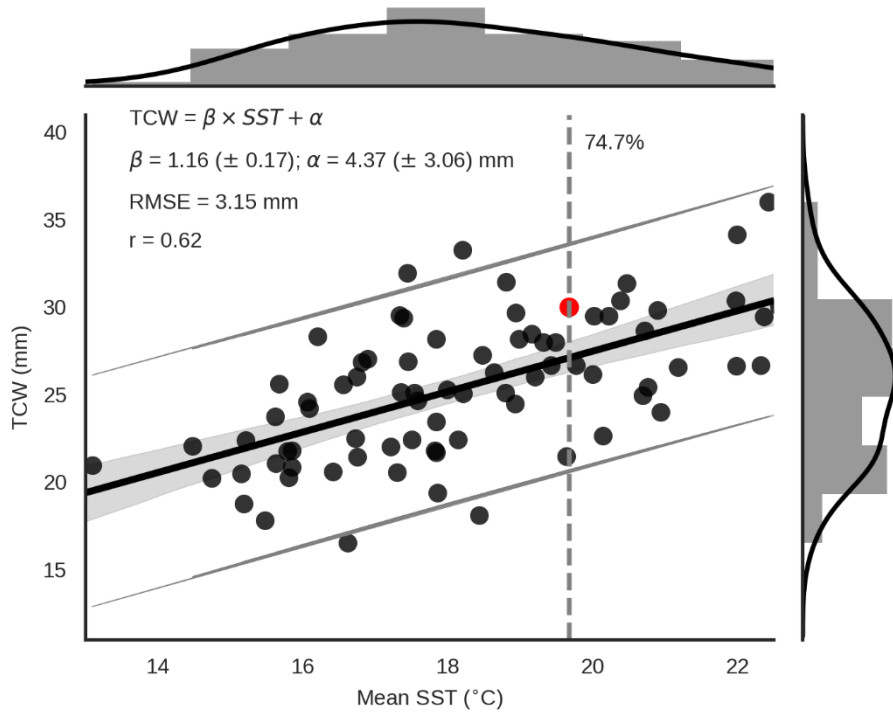
Figure 7. Relationship between the uptake-weighted SST at air parcel uptake locations, and the *TCW* upon AR landfall. The red marker indicates storm Desmond, whilst the dotted, vertical line highlights its mean SST, with the associated percentile annotated. Note that the equation of the best linear fit is indicated in the annotation, along with parameter estimates and their associated standard errors (brackets). 'RMSE' denotes the root mean square error between observed and regression-modelled *TCW,* and 'r' is the corresponding. The grey shading spans the 95% confidence interval for the regression function, and the (sub-horizontal) grey lines bracket the 95th confidence interval for the regression prediction; histograms show the marginal distributions of SST and *TCW*.
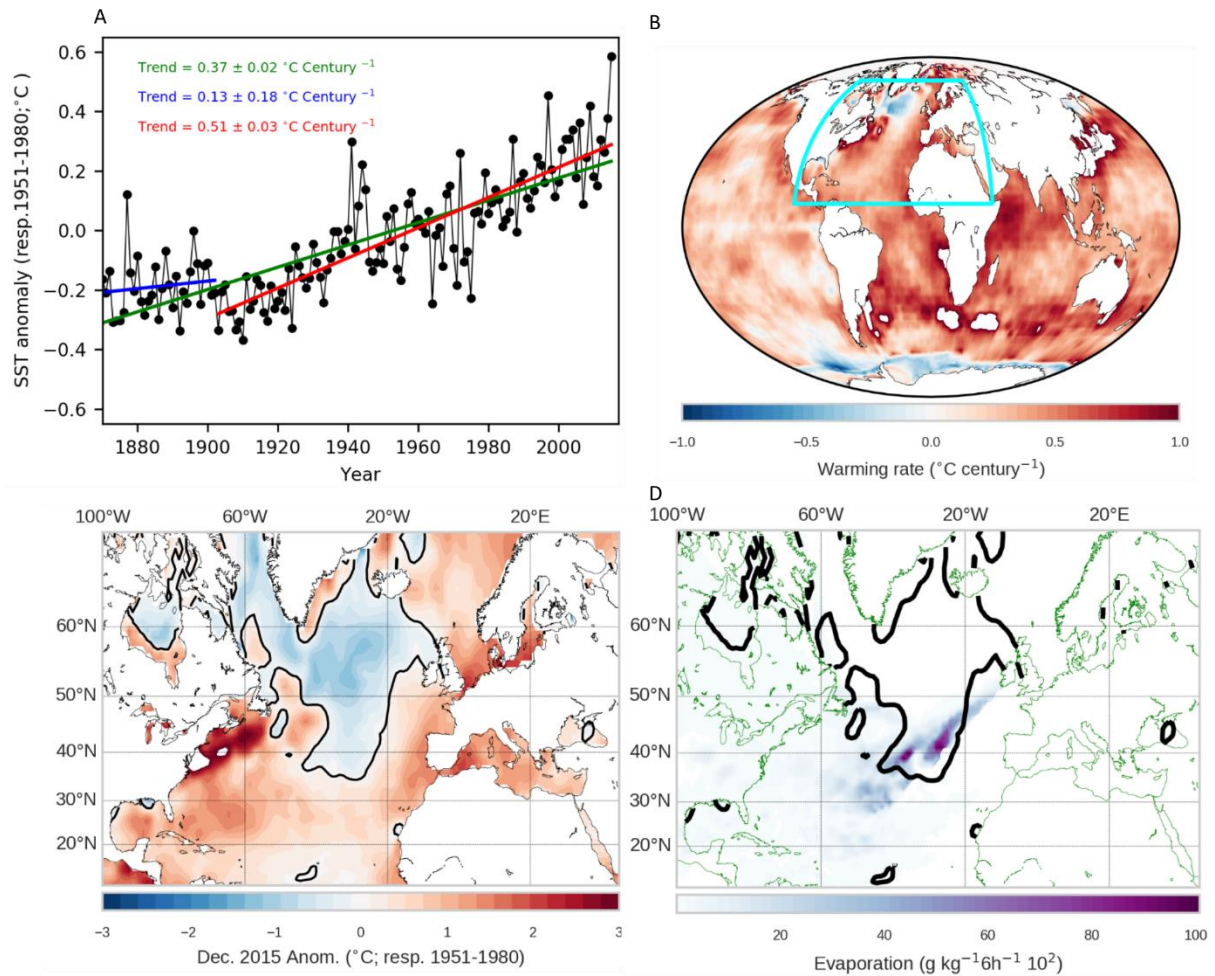
Figure 8. SSTs trends and moisture uptake locations. A: Time series of the global mean December SST, with linear trend lines fitted. The value of the slope (± one standard error) are annotated. The break point (1902) used to separate earlier and later parts of the record for trend estimation was identified as the year yielding the lowest overall RMSE for regression models fitted separately to data either side of this point. B: Trends in HadISST mean December SST over the period 1870-2015. C: December 2015 SST anomalies calculated with respect to the 1951-1980 climatology. The solid black lines highlight the zero contour. D: As in 6D, but zoomed into the North Atlantic and including the zero contour from panel C. Note that the domains plotted in C and D are marked in by the cyan rectangle.
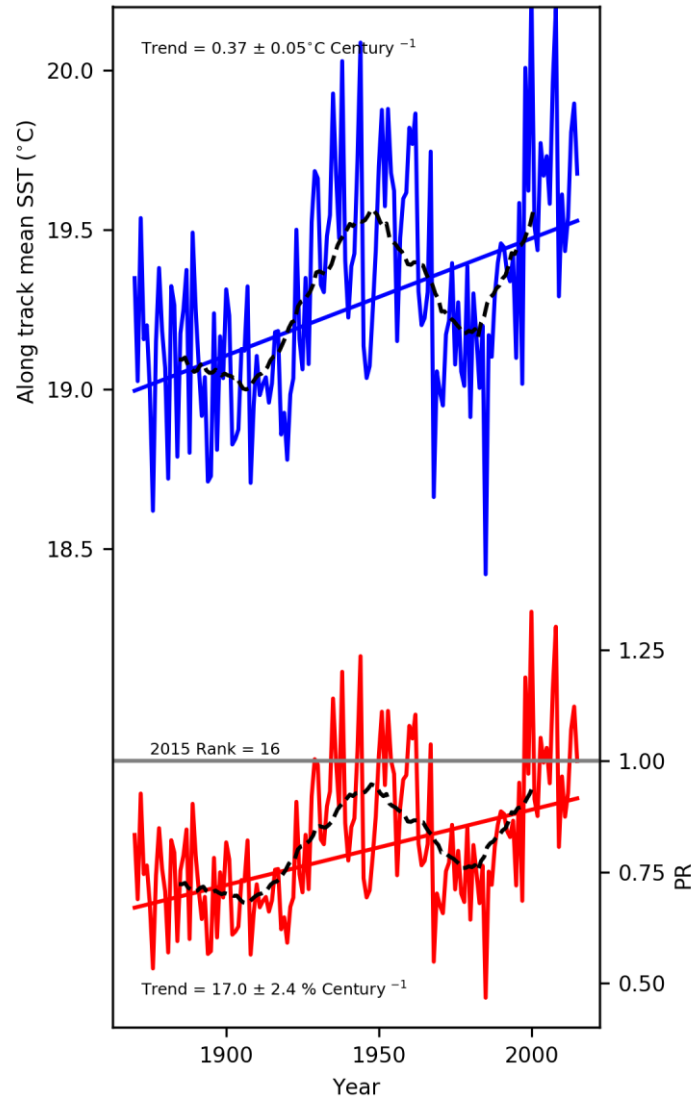
Figure 9. Time series of uptake-weighted mean SST (top) and the PR (see text), obtained by sampling SSTs at the uptake locations of air parcels entrained in Desmond's AR. Black, dashed line indicates a 30-year running mean. The slopes (annotated) were computed using the Theil-Sen method, and are highly-significant (p <0.01) according to a block-resampling bootstrap, with block lengths decided using the implicit equation given by Wilks (2011). Uncertainty in the slopes is reported as ± one standard error of the ensemble of slopes returned by the Theil-Sen algorithm.